Magnetotransport properties of MoP_2

Aifeng Wang (王爱峰),[1] D. Graf,[2] Aaron Stein,[3] Yu Liu (刘育),[1] Weiguo Yin (尹卫国),[1] and C. Petrovic[1]
[1]*Condensed Matter Physics and Materials Science Department, Brookhaven National Laboratory, Upton, New York 11973, USA*
[2]*National High Magnetic Field Laboratory, Florida State University, Tallahassee, Florida 32306-4005, USA*
[3]*Center for Functional Nanomaterials, Brookhaven National Laboratory, Upton, New York 11973-5000, USA*
(Received 28 June 2017; revised manuscript received 10 October 2017; published 2 November 2017)

We report magnetotransport and de Haas–van Alphen (dHvA) effect studies on MoP_2 single crystals, predicted to be a type-II Weyl semimetal with four pairs of robust Weyl points located below the Fermi level and long Fermi arcs. The temperature dependence of resistivity shows a peak before saturation, which does not move with magnetic field. Large nonsaturating magnetoresistance (MR) was observed, and the field dependence of MR exhibits a crossover from semiclassical weak-field B^2 dependence to the high-field linear-field dependence, indicating the presence of Dirac linear energy dispersion. In addition, a systematic violation of Kohler's rule was observed, consistent with multiband electronic transport. Strong spin-orbit coupling splitting has an effect on dHvA measurements whereas the angular-dependent dHvA orbit frequencies agree well with the calculated Fermi surface. The cyclotron effective mass $\sim 1.6 m_e$ indicates the bands might be trivial, possibly since the Weyl points are located below the Fermi level.

DOI: 10.1103/PhysRevB.96.195107

I. INTRODUCTION

Weyl fermions in condensed-matter systems have attracted considerable interest and are intensively studied [1–3]. Two types of Weyl fermions were found in solid materials. Type-I Weyl semimetal (WSM) has an ideal Weyl cone in the electronic structure and a closed pointlike Fermi surface with Lorentz symmetry, while type-II WSM has a strongly tilted Weyl cone where the Fermi surface consists of an electron and a hole pocket that touch at the Weyl node in a topologically protected manner [4,5]. Thus, type-II WSM could have some exotic properties, such as anisotropic chiral anomaly, anomalous Hall effect, and Klein tunneling [4,6,7].

The two originally proposed type-II WSM materials are WTe_2 and $MoTe_2$ [4,8]. However, the arrangement of Weyl points (WPs) is very sensitive to crystal structure. The proximity of WPs with opposite Chern numbers, and the WPs' location above the Fermi level makes WPs in WTe_2 and $MoTe_2$ unstable and difficult to probe [8]. WSM can be obtained by either breaking time-reversal symmetry or space-inversion symmetry in a Dirac semimetal [9]. MoP_2, with a similar chemical formula and nonsymmorphic space group $Cmc2_1(36)$, serves as a good candidate for a type-II WSM. Recently, MoP_2 was predicted to be a type-II WSM with stable WPs located below the Fermi level and long Fermi arcs, which can be studied by angle-resolved photoemission spectroscopy (ARPES) measurements [10].

In this paper, we have successfully grown single crystals of MoP_2, and performed magnetotransport and de Haas–van Alphen (dHvA) measurements. We found that a peak appears in the temperature dependence of resistivity at 45 K that does not change in magnetic fields up to 9 T. With increasing magnetic field, magnetoresistance (MR) exhibits a crossover from semiclassical B^2 dependence to the linear-field dependence at critical field B^*; the B^* can be described by quadratic behavior for quantum limit with linear energy dispersion. Moreover, a systematic violation of Kohler's rule was observed. The effective mass detected by dHvA is $m \cong 1.6 m_e$, indicating that the band probed by dHvA is relatively trivial, possibly since WPs are located below the Fermi level. Though the crystal structure of MoP_2 is three-dimensional (3D) without obvious stacks of layered two-dimensional building blocks, angular-dependent dHvA measurements reveal a quasi-2D Fermi surface in MoP_2 whereas the results of the dHvA measurements agree well with the calculated Fermi surface.

II. EXPERIMENTAL DETAILS

Single crystals of MoP_2 were grown by the chemical iodine vapor transport method. Polycrystal of MoP_2 was synthesized by heating stoichiometric amounts of Mo and P powders at 500 °C for 24 h, and then 750 °C for 48 h. 1 g MoP_2 polycrystal was mixed with I_2 (15 mg/ml), and then sealed in an evacuated quartz tube. Single crystals were grown in the temperature gradient 1050 °C (source) to 950 °C (sink) for two weeks. Small needlelike single crystals with typical size 200 μm × 50 μm × 20 μm were obtained. Single-crystal x-ray diffraction (XRD) measurements were performed using a Bruker Apex II single-crystal x-ray diffractometer with Mo-K_α radiation ($\lambda = 0.071\,073$ nm) at room temperature. The elemental analysis was performed using an energy-dispersive x-ray spectroscopy (EDX) in a JEOL LSM 6500 scanning electron microscope. Electrical transport was performed using a Quantum Design PPMS-9. The dHvA effect at high magnetic field up to 18 T was measured at the National High Magnetic Field Laboratory (NHMFL) in Tallahassee. Resistivity was measured using a standard four-contact configuration. For first-principles band-structure calculations, we applied the WIEN2K [11] implementation of the full potential linearized augmented plane-wave method in the generalized gradient approximation [12] of density-functional theory with spin-orbit coupling treated in a second variational method. The basis size was determined by $R_{\mathrm{mt}} K_{\mathrm{max}} = 7$ and the Brillouin zone was sampled with a regular 19 × 19 × 11 mesh containing 600

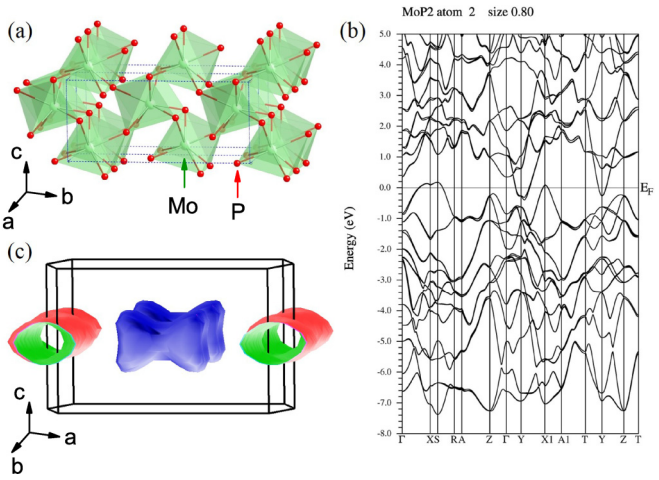

FIG. 1. (a) Crystal structure of MoP_2. (b) The band structure for MoP_2. (c) Fermi surface of MoP_2; a pair of bowtielike Fermi pockets are located around Y point in the Brillouin zone (BZ), and a pair of spaghettilike hole Fermi pockets are located at X point of BZ.

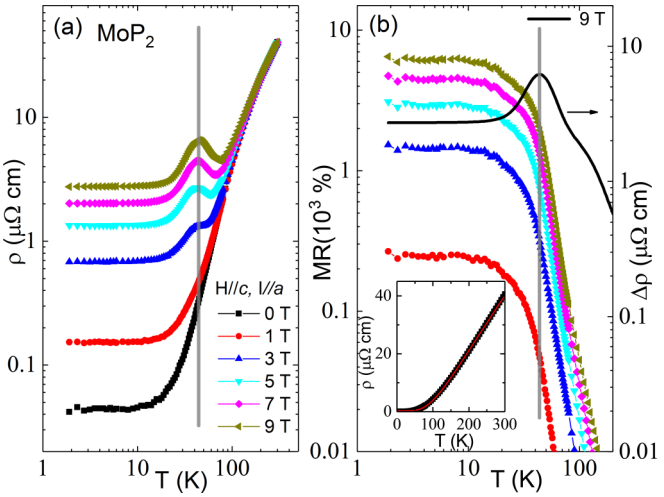

FIG. 2. (a) Temperature dependence of resistivity in different magnetic fields plotted on a log-log scale; the magnetic field is applied along c axis, and electrical current is along a axis. The grey vertical line is a guide to eye. (b) The temperature dependence of the MR $= [\rho(B) - \rho(0\ \mathrm{T})]/\rho(0\ \mathrm{T}) \times 100\%$ at different fields (left), and the $\Delta\rho = \rho(9\ \mathrm{T}) - \rho(0\ \mathrm{T})$ (right). Panels (a) and (b) use the same legend. Inset shows $\rho(0\ \mathrm{T})$ fitted with Bloch-Grüneisen model.

irreducible k points to achieve energy convergence of 1 meV. The Fermi surface was plotted in a 10 000 k-point mesh.

III. RESULTS AND DISCUSSIONS

The crystal structure of MoP_2 is shown in Fig. 1(a); each Mo atom is surrounded by seven P atoms in nearly octahedral coordination. MoP_2 with space group $Cmc2_1(36)$ is composed by the stacking of the incomplete octahedra in three directions, having a mirror plane perpendicular to the a axis, a c-glide plane perpendicular to the b axis, and a twofold screw axis parallel to the c axis. The crystal structure without space-inversion symmetry makes MoP_2 a good candidate for Weyl semimetal. The lattice parameters $a = 3.13(1)$ Å, $b = 11.12(1)$ Å, and $c = 4.94(1)$ Å determined by single-crystal XRD agree well with a previous report [13]. The average Mo : P atomic ratio determined by EDX is close to 1 : 2, consistent with the composition of MoP_2. The calculated band structure and Fermi surface of MoP_2 are shown in Figs. 1(b) and 1(c), respectively. Band splitting induced by spin-orbit coupling was observed. There is a pair of bowtielike closed electron pockets at the Y point of the Brillouin zone (BZ), and spaghettilike open hole Fermi surfaces at the X point of the BZ, which are extended along the b axis, flat along the c axis, and warped along the a axis. The band structure and Fermi surface are similar to WP_2 [10,14,15].

The temperature dependence of resistivity in different magnetic fields was measured with B parallel to the crystallographic c axis and current parallel to the a axis, as shown in Fig. 2(a). $\rho(0T)$ shows a metallic behavior with $\rho(2\ \mathrm{K}) = 0.042\ \mu\Omega\,\mathrm{cm}$ and residual resistivity ratio $= 965$, indicating the very high quality of our single crystals. The $\rho(0T)$ curve can be well fitted by the Bloch-Grüneisen (BG) model [16]:

$$\rho(T) = \rho_0 + C\left(\frac{T}{\Theta_D}\right)^5 \int_0^{\Theta_D/T} \frac{x^5}{(e^x - 1)(1 - e^{-x})} dx,$$

where ρ_0 is the residual resistivity and Θ_D is the Debye temperature. The fitting gives $\Theta_D = 591$ K, similar to that of WP_2 [17]. The good BG model fit suggests that the phonon scattering dominates in the absence of magnetic field. As shown in Fig. 2(a), a magnetic-field-induced resistivity upturn was observed at low temperature, in contrast to other semimetals such as TaAs, WTe_2, and LaSb [2,18,19]. The resistivity diminishes with further decrease in temperature and saturates below ~14 K. Peak temperature position in $\rho(T)$ at 45 K does not move with field and is shown by the vertical line in Fig. 2(a). We note that a weak peak was also observed in WP_2 [14]. Even though the peak can be observed in $\Delta\rho$, the MR monotonously increases with decreasing temperature and saturates at ~14 K, as shown in Fig. 2(b). In order to understand the peak effect we measured magnetic field dependence of MR at different temperatures.

A square to linear transition of field dependent MR was observed, and the MR can reach as high as $6.45 \times 10^3\%$ at 1.9 K and 9 T [Fig. 3(a)]. This is similar to Ta_3S_2 [20], one or two orders of magnitude smaller when compared to WTe_2 and LaSb [18,19]. According to semiclassical transport theory, if there is a single type of charge carrier and scatting in a metal, Kohler's rule states that the relative change in resistivity $\Delta\rho/\rho_0$ in a magnetic field H is a universal function of H/ρ_0, where ρ_0 is the zero-field resistivity at certain temperature [21]. As shown in Fig. 3(b), while the data below 45 K deviate from Kohler's rule, the data above 45 K still fall on the same curve, suggesting that the transport above 45 K is dominated by a single scattering process. Multiple reasons can lead to the breakdown of Kohler's law, for example a multiband effect with different scattering times. We fit the MR with a simple power law MR $= A \times H^n$; the typical data are shown in Fig. 3(c). The MR above 45 K can be well fitted in the whole range, but there are some

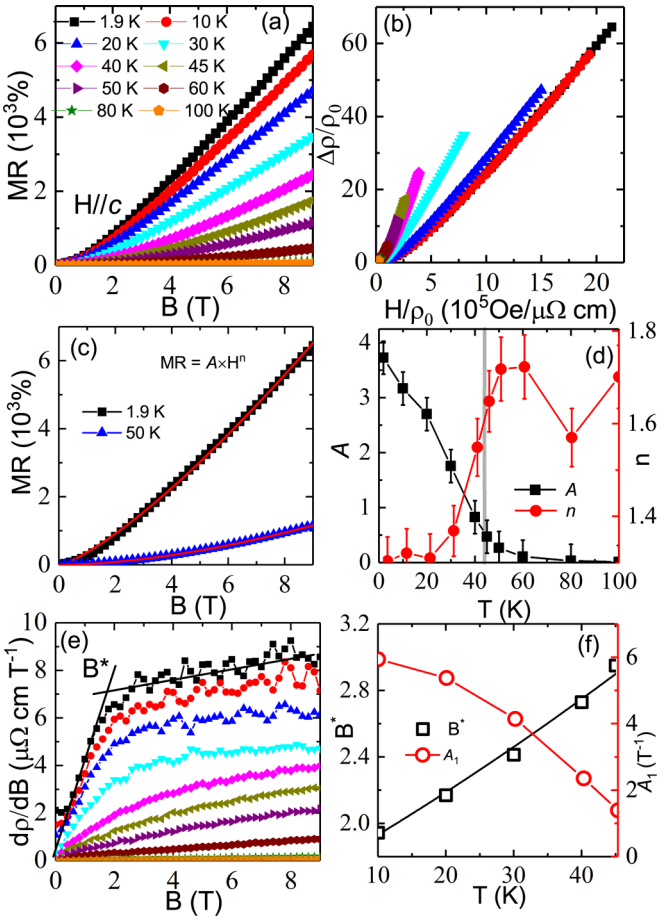

FIG. 3. (a) The MR vs magnetic field at different temperatures for MoP_2 with $H \parallel c$. (b) A Kohler plot for MoP_2. (c) Typical magnetic-field dependence of MR curves; the solid lines are fits using $\mathrm{MR} = A \times H^n$. (d) Temperature dependence of A (left) and n (right) in $\mathrm{MR} = A \times H^n$. (e) The field derivative of MR [d(MR)/dB] at different temperatures; solid lines show the criterion used to determine the critical field B^*. (f) Temperature dependence of the critical field B^* (left); the black solid line is the fitting of B^* by $B^* = \frac{1}{2e\hbar v_F^2}(E_F + k_B T)^2$. The red circle corresponds to high-field MR linear coefficient A_1.

deviations in the low-field range of the data below 45 K. The obtained parameters are shown in Fig. 3(d), A monotonously decreases with temperature increase and n increases with increasing temperature and saturates at ∼1.7. n should be 2 in a conventional metal, while linear MR is often observed in Dirac semimetals. One of the possible explanations for the temperature dependence of n is that the Dirac band plays a more important role as the temperature is lowered. Assuming similarity with WP_2, the carrier density of MoP_2 might be relatively high [17]. Due to the small effective mass and long mean free path, Dirac fermions are likely to show their footprint in the exponent of field-dependent MR reduced from the square.

A peak was observed in the temperature dependence of $\Delta\rho = [\rho(T,H) - \rho(T,0)]$ in pure metals such as copper, aluminum, and indium, which can be explained by the two-band model [22–24]. This mechanism is not likely to cause the peak observed in MoP_2 since the peak temperature in

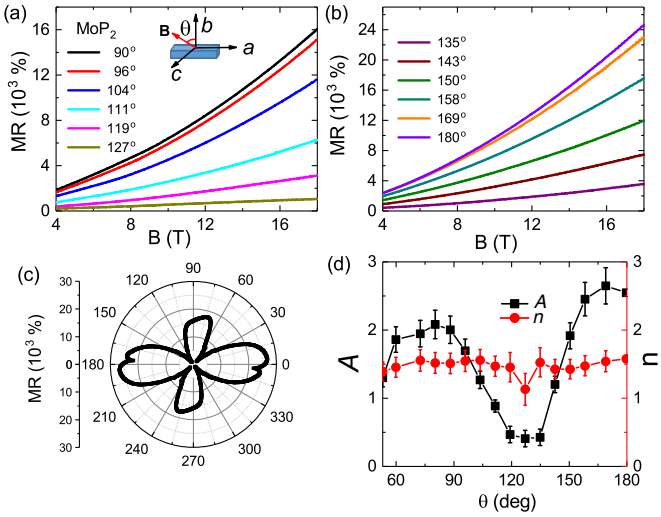

FIG. 4. (a),(b) Magnetic-field dependence of MR with field at different angles in bc plane. The current is along a axis and always perpendicular to the field. (c) Polar plot of the angular dependence of the MR with the field rotated in bc plane at 2 K and 18 T. (d) Temperature dependence of A (left) and n (right) in $\mathrm{MR} = A \times H^n$.

pure metals increases with increasing field, in contrast to the nearly magnetic-field-independent peak in MoP_2. The peak also cannot be explained by the graphitelike superconducting correlations in the quantum limit since it also increases with increasing field [25]. On the other hand, systematic evolution of A and n [Fig. 3(d)] suggests that the peak might be the result of interplay of the temperature-dependent weight of linear MR and square MR, i.e., Dirac and normal fermions.

In order to characterize the crossover behavior from weak-field B^2 dependence to the high-field linear dependence, we present the field derivative of the MR, dMR/dB, in Fig. 3(e). Linear field dependencies for dMR/dB in low fields agree with the semiclassical $\mathrm{MR} \sim A_2 B^2$. With field increasing, dMR/dB reduces from linear behavior to a weak field dependence saturating behavior above a characteristic field B^*, indicating that MR is dominated by a linear field dependence plus a small quadratic term [$\Delta\rho/\rho = A_1 B + o(B^2)$] at the high-field region [26,27]. Since the splitting between the lowest and first Landau level (LL) for the Dirac state is described as $\Delta_{LL} = \pm v_F\sqrt{2e\hbar B}$, where $\Delta_{LL} = \frac{e\hbar B}{m^*}$ for a conventional parabolic band, the quantum limit is easily reached for the Dirac band [26]. As shown in Fig. 3(f), B^* can be described by a critical field for a quantum limit at a specific temperature $B^* = \frac{1}{2e\hbar v_F^2}(E_F + k_B T)^2$ [28], suggesting that the linear MR likely originates from the Dirac states.

Figures 4(a) and 4(b) show the MR with field tilted from the c axis to the b axis. The MR at 2 K and 18 T is 1.6×10^4% along the c axis, and 2.5×10^4% along the b axis. Angular dependence of the MR with the magnetic field perpendicular to the electric current is shown in Fig. 4(c). In contrast to WP_2 where the angular dependence of MR shows 2D behavior [14,15,17], MoP_2 shows fourfold symmetry. The different bc plane symmetry and similarity of Fermi surfaces of MoP_2 and WP_2 indicate that the transport properties are sensitive to the fine details of Fermi surface and/or the spin-orbital

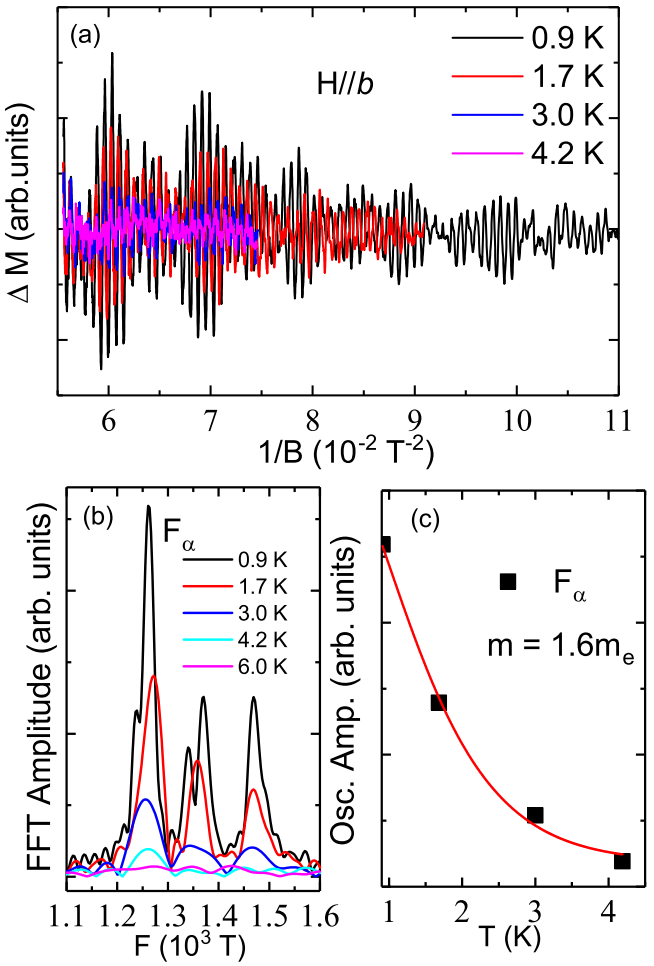

FIG. 5. (a) dHvA oscillatory components at different temperatures obtained by subtracting smooth background. (b) FFT spectra for the dHvA oscillations in (a). (c) Temperature dependence of the oscillating amplitude at $F_\alpha = 1261$ T, solid line is fitted using Lifshitz-Kosevich formula.

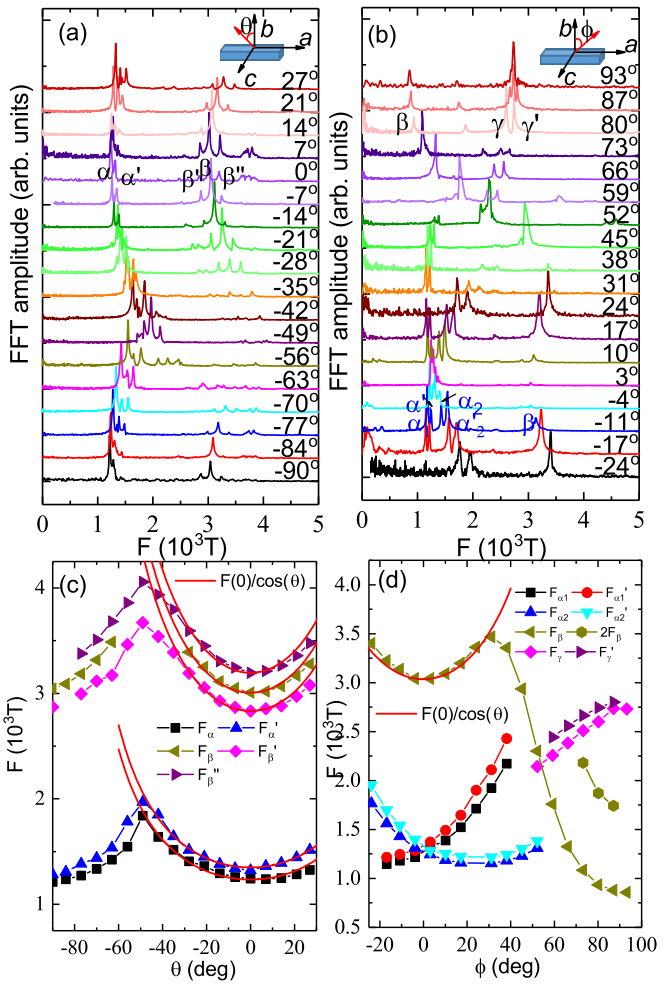

FIG. 6. FFT spectra of dHvA oscillaiton with field rotated in the bc plane (a) and in the ab plane (b); the spectra are normalized and shifted vertically for clarity. (c),(d) Angular dependence of the oscillation frequency corresponding to the oscillation in (a) and (b), respectively. Red solid lines are fits with 2D model $F(0)/\cos(\theta)$.

coupling. We also fit the MR at different angles with power law MR $= A \times H^n$, as shown in Fig. 4(d). Whereas A shows similar angular dependence as MR amplitude does, n is nearly constant with angle.

Quantum oscillation is a powerful tool in investigating Weyl/Dirac materials. We measured de Haas–van Alphen (dHvA) oscillations in MoP_2 at different temperatures, as shown in Fig. 5(a). Beat patterns were observed, indicating that multiple frequencies contribute to the oscillations. The corresponding fast Fourier transform (FFT) spectra are shown in Fig. 5(b), similar to that of WP_2. Three frequencies are observed: 1261, 1371, and 1469 T. According to the Onsager relation, $F = (\Phi_0/2\pi^2)A_F$, where Φ_0 is the flux quantum and A_F is the orthogonal cross-sectional area of the Fermi surface; the Fermi surface is estimated to be 12, 13, and 14 nm^{-2}. This corresponds to 4.7%, 5.1%, and 5.5% of the total area of the Brillouin zone in the ac plane. The oscillations dampen quickly with temperature and disappear above 4.2 K, indicating a heavy cyclotron mass in MoP_2. The temperature dependence of the amplitude of the oscillations is fitted using the Lifshitz-Kosevich formula [29], $A \sim [\alpha m^*(T/B)/\sinh(\alpha\, m^* T/B)]$ where $\alpha = 2\pi^2 k_B/e\hbar \approx 14.69$ T/K and $m^* = m/m_e$ is the cyclotron mass ratio (m_e is the mass of free electron), as exhibited in Fig. 5(c). The fitting gives $m^* \cong 1.6$, similar to that in WP_2, possibly due to electron-phonon many-body interactions [14]. The effective cyclotron mass suggests that the band detected by the dHvA effect might be trivial, in agreement with the location of the Weyl points below the Fermi level [10]. The trivial Fermi surfaces are not consistent with the Dirac states indicated by linear MR. A possible explanation is that the Dirac state usually leads to a small Fermi surface and therefore might not be easily detected by dHvA measurement. This is similar to the case in MoP, where a triply degenerate point with Dirac-like dispersion well below the Fermi level has been discovered [30].

Angular-dependent dHvA oscillations provide further insights into Fermi-surface properties. The FFT spectra of dHvA oscillations are shown in Figs. 6(a) and 6(b) for magnetic field rotated in the bc and ab planes, respectively. The positions of the FFT peaks are summarized in Figs. 6(c) and 6(d). The FFT peaks can be generally divided into two groups, one group

around 1200 T, and another group around 3000 T. According to the calculated Fermi surface, as shown in Fig. 1(c), lower frequencies around 1200 T should arise from the oscillation of a spaghettilike open hole Fermi surface, while higher frequencies around 3000 T are due to the oscillation of a bowtielike closed electron Fermi surface. Split peaks and small peaks around the main peaks might be due to strong spin-orbit coupling and warped Fermi surface [14]. Even though the crystal structure is three dimensional and quite different from the quasi-2D structure of $SrMnBi_2$ with square Bi layers [26], all peaks show quasi-2D angle dependence $[F(0)/\cos(\theta)]$ at low angles around $H \parallel b$, indicating a quasi-2D Fermi surface (FS) in MoP_2 [Fig. 6(c)]. The peaks show symmetry behavior at $\sim 50^\circ$, indicating possible fourfold symmetry in the bc plane, consistent with the fourfold symmetry of MR in the bc plane. When the magnetic field is rotated in the ab plane, peaks corresponding to the hole pocket show behavior of two elliptical FSs enlongated $\sim 25^\circ$ away from the b axis. This is consistent with the calculated spaghettilike hole pocket [10,14]. As shown in Fig. 1(c), the spaghettilike hole pocket is flat along the ab plane, indicating quasi-2D-like behavior with the magnetic field rotated in the bc plane, while it is rather warped in the bc plane with two hole pockets bent at opposite directions. This gives rise to the behavior in Fig. 6(d). F_β also shows quasi-2D angle dependence with the field rotated in the ab plane with $\phi \leqslant 30^\circ$, however, with further increase, the angle F_β decreases quickly to 856 T at $\phi = 90^\circ$ ($H \parallel a$). This can be explained by the bowtielike electron pocket, when $\phi \leqslant 30^\circ$; quantum oscillations are due to the orbit crossing all the pocket—the flat side wall gives rise to quasi-2D behavior. When $\phi > 30^\circ$ quantum oscillations are due to the orbit on the neck of the bowtie, which decreases quickly with angle and shows minimum value with $\phi = 90^\circ$ ($H \parallel a$), even smaller than hole pocket [10,14]. The Fermi surface measured by dHvA agrees well with the theoretical calculation, giving indirect support for the band structure and predicted type-II Weyl points [10].

In addition to charge compensation, spin-orbital coupling and the related spin and orbital angular momentum texture also play an important role in large MR in WTe_2 [31]. The spin textures can reduce the resistivity by suppressing the backscattering channel of the quasiparticles, and large MR is observed when the external magnetic field changes the spin structure and lifts the scattering protection. The carrier density in WP_2 is relatively high [15,17], and the spin texture might be important for the large MR in WP_2. Moreover, WP_2 crystal structure lacks weakly van der Waals bonded layers, yet still features a Fermi surface with 2D angular dependence of MR. This might be attributed to the spin textures, which show large anisotropy [31]. Assuming the circular cross section of the hole Fermi pockets, the spin-orbital coupling induced band splitting in MoP_2 is estimated to be $k_{\alpha'} - k_\alpha = 6.0 \times 10^{-3}$ Å^{-1}, similar to that in MoP and smaller than 3.2×10^{-2} Å^{-1} in WP_2 [17,32]. As a result, the different values of MR and the angular dependence of MR can be explained by the strength of spin-orbital coupling. Our measurements indicate that strong spin-orbital coupling plays an important role in the transport properties of MoP_2, which requires additional studies.

IV. CONCLUSIONS

In conclusion, our MR studies are consistent with the presence of both Dirac states and the parabolic band with enhanced quasiparticle mass in MoP_2. The dHvA measurements reveal quasi-2D multiband transport and are in agreement with the calculated Fermi surface. Strong spin-orbital coupling is rather important in the electronic transport of MoP_2.

ACKNOWLEDGMENTS

We thank D. Szalda for help with Bruker APEXII measurements and J. Warren for his help with scanning electron microscopy measurements. Work at BNL was supported by the U.S. DOE-BES, Division of Materials Science and Engineering, under Contract No. DE-SC0012704. Work at the National High Magnetic Field Laboratory was supported by NSF Cooperative Agreement No. DMR-1157490, and by the state of Florida.

[1] H. Weng, C. Fang, Z. Fang, B. A. Bernevig, and X. Dai, Phys. Rev. X **5**, 011029 (2015).
[2] X. Huang, L. Zhao, Y. Long, P. Wang, D. Chen, Z. Yang, H. Liang, M. Xue, H. Weng, Z. Fang, X. Dai, and G. Chen, Phys. Rev. X **5**, 031023 (2015).
[3] S. Y. Xu, I. Belopolski, N. Alidoust, M. Neupane, G. Bian, C. L. Zhang, R. Sankar, G. Q. Chang, Z. J. Yuan, C. C. Lee, S. M. Huang, H. Zheng, J. Ma, D. S. Sanchez, B. K. Wang, A. Bansil, F. C. Chou, P. P. Shibayev, H. Lin, S. Jia, and M. Z. Hasan, Science **349**, 613 (2015).
[4] A. A. Soluyanov, D. Gresch, Z. Wang, Q. Wu. M. Troyer, X. Dai, and B. A. Bernevig, Nature (London) **527**, 495 (2015).
[5] Y. Xu, F. Zhang, and C. Zhang, Phys. Rev. Lett. **115**, 265304 (2015).
[6] A. A. Zyuzin and R. P. Tiwari, JETP Lett. **103**, 717 (2016).
[7] T. E. O'Brien, M. Diez, and C. W. J. Beenakker, Phys. Rev. Lett. **116**, 236401 (2016).
[8] Z. Wang, D. Gresch, A. A. Soluyanov, W. Xie, S. Kushwaha, X. Dai, M. Troyer, R. J. Cava, and B. A. Bernevig, Phys. Rev. Lett. **117**, 056805 (2016).
[9] B. Yan and C. Felser, Annu. Rev. Condens. Matter Phys. **8**, 337 (2017).
[10] G. Autes, D. Gresch, M. Troyer, A. A. Soluyanov, and O. V. Yazyev, Phys. Rev. Lett. **117**, 066402 (2016).
[11] K. Schwarz, P. Blaha, and G. K. H. Madsen, Comput. Phys. Commun. **147**, 71 (2002).
[12] J. P. Perdew, K. Burke, and M. Ernzerhof, Phys. Rev. Lett. **77**, 3865 (1996).
[13] S. Rundqvist and T. Lundstrom, Acta Chem. Scand. **17**, 37 (1963).
[14] N. Kumar, Y. Sun, K. Manna, V. Süss, I. Leermakers, O. Young, T. Förster, M. Schmidt, B. Yan, U. Zeitler, C. Felser, and C. Shekhar, arXiv:1703.04527.

[15] R. Schönemann, N. Aryal, Q. Zhou, Y.-C. Chiu, K.-W. Chen, T. J. Martin, G. T. McCandless, J. Y. Chan, E. Manousakis, and L. Balicas, Phys. Rev. B **96**, 121108 (2017)..
[16] M. Ziman, *Electrons and Phonons* (Clarendon, Oxford, 1962).
[17] A. Wang, D. Graf, Yu Liu, Q. Du, J. Zheng, H. Lei, and C. Petrovic, Phys. Rev. B **96**, 121107(R) (2017).
[18] M. N. Ali, J. Xiong, S. Flynn, J. Tao, Q. D. Gibson, L. M. Schoop, T. Liang, N. Haldolaarachchige, M. Hirschberger, N. P. Ong, and R. J. Cava, Nature (London) **514**, 205 (2014).
[19] F. F. Tafti, Q. D. Gibson, S. K. Kushwaha, N. Haldolaarachchige, and R. J. Cava, Nat. Phys. **12**, 272 (2015).
[20] D. Chen, L. X. Zhao, J. B. He, H. Liang, S. Zhang, C. H. Li, L. Shan, S. C. Wang, Z. A. Ren, C. Ren, and G. F. Chen, Phys. Rev. B **94**, 174411 (2016).
[21] A. B. Pippard, *Magnetoresistance in Metals* (Cambridge University Press, Cambridge, England, 1989).
[22] M. L. Snodgrass, F. J. Blatt, Jon L. Opsal, and C. K. Chiang, Phys. Rev. B **13**, 574 (1976).
[23] J. E. Huffman, M. L. Snodgrass, and F. J. Blatt, Phys. Rev. B **23**, 483 (1981).
[24] R. J. Schwartz and F. Stangler, Phys. Status Solidi B **60**, K69 (1973).
[25] Y. Kopelevich, J. H. S. Torres, R. R. da Silva, F. Mrowka, H. Kempa, and P. Esquinazi, Phys. Rev. Lett. **90**, 156402 (2003).
[26] K. Wang, D. Graf, Hechang Lei, S. W. Tozer, and C. Petrovic, Phys. Rev. B **84**, 220401 (2011).
[27] H.-H. Kuo, J. H. Chu, S. C. Riggs, L. Yu, P. L. McMahon, K. De Greve, Y. Yamamoto, J. G. Analytis, and I. R. Fisher, Phys. Rev. B **84**, 054540 (2011).
[28] K. K. Huynh, Y. Tanabe, and K. Tanigaki, Phys. Rev. Lett. **106**, 217004 (2011).
[29] D. Shoeneberg, *Magnetic Oscillation in Metals* (Cambridge University Press, Cambridge, England, 1984).
[30] B. Q. Lv, Z.-L. Feng, Q.-N. Xu, X. Gao, J.-Z. Ma, L.-Y. Kong, P. Richard, Y.-B. Huang, V. N. Strocov, C. Fang, H.-M. Weng, Y.-G. Shi, T. Qian, and H. Ding, Nature (London) **546**, 627 (2017).
[31] J. Jiang, F. Tang, X. C. Pan, H. M. Liu, X. H. Niu, Y. X. Wang, D. F. Xu, H. F. Yang, B. P. Xie, F. Q. Song, P. Dudin, T. K. Kim, M. Hoesch, P. K. Das, I. Vobornik, X. G. Wan, and D. L. Feng, Phys. Rev. Lett. **115**, 166601 (2015).
[32] C. Shekhar, Y. Sun, N. Kumar, M. Nicklas, K. Manna, V. Suess, O. Young, I. Leermakers, T. Förster, M. Schmidt, L. Muechler, P. Werner, W. Schnelle, U. Zeitler, B. Yan, S. S. P. Parkin, and C. Felser, arXiv:1703.03736.